A Core@sheath Nanofibrous Separator for Lithium Ion Batteries Obtained by Coaxial Electrospinning[a,b]

Zhihong Liu, Wen Jiang, Qingshan Kong, Chuanjian Zhang, Pengxian Han, Xuejiang Wang, Jianhua Yao, Guanglei Cui*

A composite core@sheath nanofibrous separator for lithium ion batteries is fabricated via coaxial electrospinning, using thermosetting PI as the core material and PVDF-HFP as the sheath material. It is demonstrated that the PI@PVDF-HFP nonwovens display remarkably improved tensile strength up to 53 MPa and high thermal stability up to 300 °C. The electrochemical characterization shows that cells using core@sheath nonwovens as separators display better rate capability and better cycling capacity retention. Considerable mechanical strength, higher thermal stability and preferable rate capability might make this kind of core@sheath nonwovens promising separators for higher-power application.

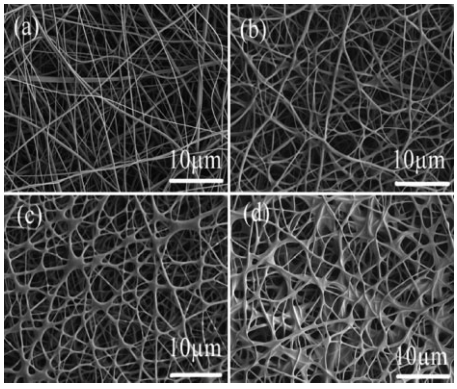

1. Introduction

As high-power lithium ion batteries are rapidly stepping into a promising field such as electric vehicles, the safety issue of these high-power batteries attracts extensive attention.[1–5] To avoid internal short circuit failure, a robust separator should play a significant role in securing battery safety. Polyolefin microporous membranes such as polyethylene (PE) and poly(propylene) (PP) have been commercially available as major separators for lithium ion battery.[1,2] However, these polyolefin-based separators suffer from poor wettability, poor thermal shrinkage and low transverse mechanical strength.[6–20] The poor wettability impairs the power capability and cycle life of the battery, and brings additional disadvantages in the manufacturing speed. To improve the wettability, a polydopamine (DPA) treatment was developed in addition to the plasma surface treatment technology.[6–8] The poor thermal shrinkage and low transverse mechanical strength of PE or PP separator have aroused serious concern on internal electrical short circuit at high discharge rates or under vigorous conditions such as abnormal heating and mechanical rupture. Many efforts have been made to improve the thermal stability and mechanical strengths using composite or hybrid materials, such as incorporating inorganic particles onto the surface of commercialized separators[9–13] or adopting heat resistant polymers, e.g., polyacrylonitrile (PAN),[14–17] poly(ethylene terephthalate) (PET),[18–20] polyimide (PI)[21] and poly(*p*-phenylene terephthalamide) (PPTA)[22] as building blocks to reinforce the thermal stability. Among them, a number of composite separators or gel electrolytes were made by a dip-coating or blade-coating on the microporous substrates, e.g., PE/poly(ethylene oxide) (PEO) and PEO/poly[(vinylidene fluoride)-*co*-hexafluoropropene] (PVDF-HFP),[13] PET/SiO_2 and PET/PVDF-HFP,[18] PET/PVDF-HFP[19] and PET/poly(methyl

Z. Liu, W. Jiang, Q. Kong, C. Zhang, P. Han, X. Wang, J. Yao, G. Cui
Qingdao Institute of Bioenergy and Bioprocess Technology, Chinese Academy of Sciences, 266101 Qingdao, China
E-mail: cuigl@qibebt.ac.cn

[a] **Supporting Information** for this article is available from the Wiley Online Library or from the author.

[b] Z. Liu and W. Jiang contributed equally to this work.

DOI: 10.1002/mame.201200158

methacrylate) (PMMA).[20] However, it is a great challenge to obtain a homogeneous coating inside microporous substrates.

In recent years electrospinning technique has been developed as a facile procedure to fabricate uniform nano-sized fibers, which is gaining intensive interest in the preparation of nonwoven separator for lithium ion battery. Electrospun membranes of polymeric electrolytes or separators were shown to improve ionic conductivity and electrochemical performance when compared to those commercialized separators.[23] Their performance enhancement is originated from the homogeneous and nano-scaled morphology. Since Locertales et al. initially proposed a coaxial electrospinning technique for the preparation of core@sheath nanofibers in 2002,[24] composite nanofibers with a core@sheath structure have gained increasing attention in the fields[25–31] such as light-guiding nanofibers,[26] conductive nanofibers,[31] drug delivery carriers[28,30] and phase change systems.[29] Combined advantages or functionalities can be anticipated owing to the coaxially compositing of different materials in the radial direction. For separator issue, the core material can be designed to provide superior thermal and mechanical properties, while the sheath can be tailored to deliver additional characteristics, such as excellent chemical resistance and ion transportation. To the best of our knowledge, the composite core@sheath nanofibers have not yet been reported for battery separators by this coaxial electrospinning technique. Inspired by the combined performance as well as its compatibility with the facile coaxial electrospinning process, herein we present our research on PI@PVDF-HFP nonwoven separator of lithium ion battery. High performance polyimide was used as the core material due to its superior thermal stability over PE, PP, PAN and PET. PVDF-HFP was chosen for the sheath material because of good affinity with liquid electrolyte. It was anticipated that the core@sheath structure could deliver perfect performance owing to the synergistic characteristic. By tuning the structure of PI@PVDF-HFP nanofibers, the thermal, mechanical and electrochemical properties of the separator were discussed in details.

2. Experimental Section

2.1. Materials and Measurements

N,N-dimethylformamide (DMF, 99.5%, Tianjin Fuyu Chem. Co.), *N,N*-dimethylacetamide (DMAc, 99.5%, Tianjin Fuyu Chem. Co.), pyromellitic dianhydride (PDA, ≥98.5%, Sinopharm. Chemical Reagent Co.), 4,4′-diaminophenyl ether (ODA, 98%, Alfa Aesar) and PVDF-HFP (Aldrich, $M_w \approx 400\,000$) were commercially available and used without further purification. Inherent viscosity of PI precursor PDA-ODA(poly(amide acid) of PDA and ODA) was measured using an Ubbelohole Viscometer ($\Phi = 0.8$–0.9 mm) in dimethylacetamide (DMAc) at 25 °C.

2.2. Synthesis of PI Precursor PDA-ODA

The synthesis of polyimide and its precursor is shown in Scheme S1 of Supporting Information. The typical polymerization of PI precursor is described briefly as follows. Equimolar amounts of PDA (4.3624 g, 0.02 mol) and ODA (4.0048 g, 0.02 mol) and some DMAc solvent were mixed in a 250 mL four-necked flask equipped with a mechanical stirrer under argon atmosphere at 0 °C for 24 h to give the highly sticky poly(amide acid) solution (20 wt%. The inherent viscosity of the polymer product was measured to be 2.11 dL · g^{-1} by diluting the as-synthesized highly sticky solution into dilute DMAc solution. The as-synthesized sticky precursor PDA-ODA solution was kept in a refrigerator for further use.

2.3. Coaxial Electrospinning and Preparation of the PI@PVDF-HFP Nanofibrous Separator

The coaxial electrospinning process was performed by using the above precursor PDA-ODA solution for the core solution and 25 wt% PVDF-HFP solution in DMF for the sheath solution. The electrospinning equipments are mainly comprised of a high voltage power supply (Spellman SL150, USA), two syringe pumps (New Era Pump system NE-1600, USA), a spinneret consisting of two chambers and a collector. The nozzle at the tip of the spinneret includes two circular channels and the configuration was shown in Figure S1 of Supporting Information. A 25 kV electrical potential is applied to a 25 cm distance between the spinneret and the collector. The speed of the core solution supply was fixed at 0.4 mL · h^{-1}, while the feed rates of the sheath solution varied from 0.16, 0.24 to 0.4 mL · h^{-1}. The as-electrospun PDA-ODA@PVDF-HFP nanofibers were collected in a form of nonwoven sheets on the aluminum foil as a collector.

The imidization of core component from PDA-ODA to PI was carried out in an oven by the following steps: (i) heating up to 100 °C for 30 min to remove the residue solvent; (ii) heating up to 200 °C and keeping stayed for 30 min; (iii) heating up to 300 °C and keeping stayed for 30 min. The imidization procedure was monitored by the infrared spectroscopy (IR) conducted on a Nicolet iN10 spectrophotometer. The samples for IR measurements were consisted of just a few lays of nanofibers. After thermal imidization, the nonwoven mats were mechanically pressed on a preforming machine (769YP-24B, Tianjin) under 5 MPa oil pressure for 3 min to provide the PI@PVDF-HFP separators with 35 μm thickness. The procedure for the entire preparation is illustrated in Scheme 1.

2.4. Characterization of the PI@PVDF-HFP Nonwoven Separator

The microporous morphology, air permeability, mechanical strength and thermal shrinkage of separators are the major characteristics that should be carefully monitored. The surface morphologies of separators were examined using a Hitachi S-4800 field emission scanning electron microscope (SEM). The air permeability was examined with a Gurley densometer (4110N, Gurley) by measuring the time necessary for air to pass through a determined volume (100 cc) under a given pressure. The mechanical properties were measured using an Inston-3300 universal testing machine (USA) at a stretching speed of 1.66 mm · s^{-1} with the sample straps of about 1 cm wide and 8 cm long.

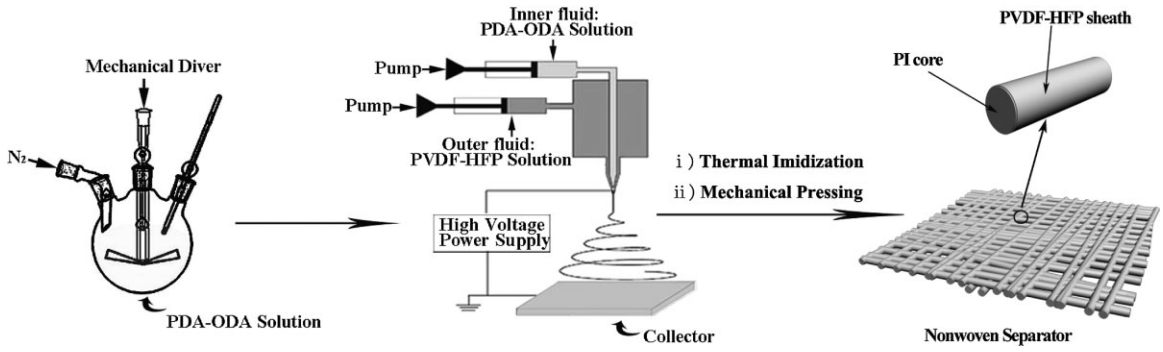

Scheme 1. Procedure for preparation of PI@PVDF-HFP nanofibrous nonwovens.

The liquid electrolyte uptake (EU) of the separators was measured by immersing the nonwovens in the liquid electrolyte [1 M lithium hexafluorophosphate ($LiPF_6$) dissolved in 1:1 v/v ethylene carbonate (EC)/dimethyl carbonate (DMC)] for 2 h. Liquid electrolyte-soaked membranes were weighed quickly after removing the excrescent solution using wipes. The EU was calculated by the equation: EU (%) $= (W_1 - W_0)/W_0 \times 100\%$, where W_1 and W_0 are the weights of the electrolyte-soaked and dry separators, respectively. The porosity of the separators was determined using butanol uptake. For this purpose, the mass of the separators was measured before and after immersion in butanol for 2 h. The porosity of the separator was calculated using the equation: porosity $= (m_b/\rho_b)/(m_b/\rho_b + m_p/\rho_p) \times 100\%$, where m_b and m_p are the mass of butanol and the separator, ρ_b and ρ_p are the density of butanol and the polymers, respectively. The thermal shrinkage of the separators was determined by measuring their dimension change after they were subjected to heat treatment in an oven at temperature of 150 °C for 1 h. Their thermal behaviors were studied by a differential scanning calorimeter (Diamond DSC, Perkin-Elmer) and a high pressure high temperature thermogravimetric analyzer (TGA, Rubotherm-DynTHERM).

2.5. Electrochemical Characterization of the PI@PVDF-HFP Nonwoven Separator

For measurement of electrochemical performance, a liquid electrolyte of 1 M $LiPF_6$ in EC/DMC (1:1 v/v) was employed. The electrochemical stability window of the separators was evaluated by a linear sweep voltammetry experiment performed on a working electrode of stainless-steel and a counter electrode of lithium metal at a scan rate of 1.0 mV · s^{-1}. The ionic conductivity of the liquid electrolyte-soaked separator between two stainless-steel plate electrodes was obtained by an AC impedance analysis using a Zahner Zennium electrochemical working station at amplitude of 10 mV over a frequency range of 1–10^6 Hz. A unit coil cell (2032-type) was assembled by sandwiching a separator between a natural graphite anode and a $LiCoO_2$ cathode and filling with liquid electrolyte. All assembly of cells was carried out in an argon-filled glove box. The charge/discharge C-rate capability and cycle ability of cells were examined using a LAND battery testing system. The discharge current densities were varied from 0.2 C (20.1 mA · g^{-1}) to 8.0 C (723.6 mA · g^{-1}) under a voltage range between 2.75 and 4.2 V. The cells were cycled at a fixed charge/discharge current density of 0.5 C (49.6 mA · g^{-1})/0.5 C (49.6 mA · g^{-1}) for cycle life testing.

The interfacial resistances between liquid electrolyte-soaked PI@PVDF-HFP nonwovens and lithium metal electrodes were measured by monitoring the impedance of symmetrical lithium cells under open-circuit conditions. The experiments were conducted on the same instrument for the ionic conductivity measurement over a frequency range of 10^6–1 Hz using two lithium electrodes instead of the stainless-steel plate electrodes.

3. Results and Discussion

3.1. Preparation of PI@PVDF-HFP Nanofibrous Nonwovens

The process parameters on coaxial electrospinning, including the viscosity, electrical conductivity, surface tension and fluid flow rates of polymer solutions have been reported to influence the surface morphology of the nanofibers.[15,32,33] In our experiment, the homogeneous morphology of PDA-ODA nanofibers could be obtained by using concentration of 20% PDA-ODA in DMAc and its inherent viscosity was 2.11 dL · g^{-1}. In this coaxial electrospinning process, the high concentration of 25% PVDF-HFP in DMF was used as the sheath solution. Though DMAc and DMF were highly miscible solvents, the high viscosity of both solutions ensured the core@sheath structure available, because high viscosity prevented any mixing of the core and sheath solutions in comparison to the fast stretching and solidification.[25] Feed rates of the core and sheath solutions were found to distinctly affect the surface morphologies of the PI@PVDF-HFP nanofibrous nonwovens as illustrated in Figure S3 of Supporting Information. So, in order to maintain the core@sheath structure after imidization reaction at 300 °C, the feed rates of core and sheath solutions were optimized to be 0.4 and 0.16 mL · h^{-1} respectively in our experiment. Infrared spectroscopy (IR) has widely been used for the chemical structure characterization during imidization reaction.[34] The infrared spectra of the pristine PDA-ODA@PVDF-HFP

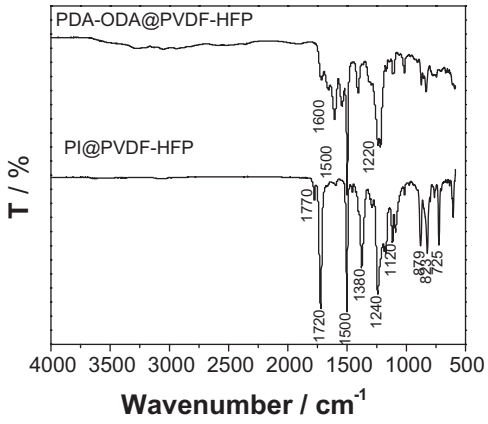

Figure 1. Fourier-transform infrared spectra of the as-electrospun PDA-ODA@PVDF-HFP nonwovens and PI@PVDF-HFP nonwovens after imidization.

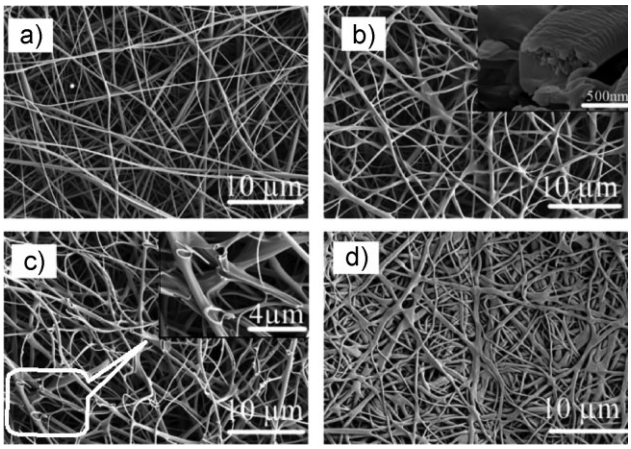

Figure 2. Typical SEM images of the core/sheath nanofibers: (a) the pristine PDA-ODA@PVDF-HFP nanofibers, (b) the as-prepared PI@PVDF-HFP nanofibrous nonwoven, (c) the broken surface morphology of PI@PVDF-HFP nanofibrous nonwoven after peeling off and (d) PI@PVDF-HFP nanofibrous nonwoven after being mechanically pressed.

and PI@PVDF-HFP nanofibers were presented in Figure 1. After curing reaction at 300 °C, the broad absorption band between 3 700 and 2 000 cm^{-1} ascribed to the stretching vibration absorption of N–H and O–H decreased drastically. And the sharp absorption peaks at 1 770 and 1 720 cm^{-1} occurred, which were related to the stretching vibration absorption of C=O in the imide structure. It was confirmed by the aforementioned IR spectra that PDA-ODA@PVDF-HFP was transformed into PI@PVDF-HFP completely. The condition of 300 °C/30 min might not be sufficient to fully imidize the poly(amic acid) for the normal casting membrane, however, in the case of nanofibers, the poly(amic acid) can be fully imidized into PI. The cyclized imide core structure could endow PI@PVDF-HFP nonwovens with higher mechanical and thermal stability.

3.2. Characterization of the Nonwoven Separator

It is observed in SEM image of Figure 2(a) that the pristine coaxial PDA-ODA@PVDF-HFP nanofibers were randomly arranged with a diameter size of around 400 nm. After imidization, the morphology of the PI@PVDF-HFP nanofibers were depicted in Figure 2(b). The sheath layer of PVDF-HFP became melted and bonded together between the nanofibers. As shown in the inset image in Figure 2(b), the cross-section of a single PI@PVDF-HFP nanofiber after quenched in liquid nitrogen manifested a core@sheath structure (also seen in Figure S4 of the Supporting Information). The diameter of the core layer was observed to be around 320 nm surrounded by the sheath layer with a thickness of around 40 nm. The melt/bonding interfaces between the fibers could be well observed when some surface fibers were removed by peeling off, which was shown in Figure 2(c). It was also manifested that the bonded sheath broke and the PI remained intact. These results further confirmed a core@sheath structure and also implied that the PI core component offered much higher mechanical strength than the PVDF-HFP sheath. It was depicted in Figure 2(d) that the pressed PI@PVDF-HFP nanofibrous nonwovens possessed uniform morphology and well-connected interstitial voids with reduced pore sizes. These tortuous small pores and uniform pore size distribution are well qualified for better performance in lithium ion battery.

The mechanical strength test results of the PI@PVDF-HFP nonwoven were presented in Figure 3. The tensile strength was 53 MPa with deformation of 57% in dry state, which was better than that of pristine PI nonvoven (30 MPa, seen in Figure S10 of Supporting Information). The unexpected robustness was attributed to the strong bonding of PI core resulting from the melted PVDF-HFP sheaths between the

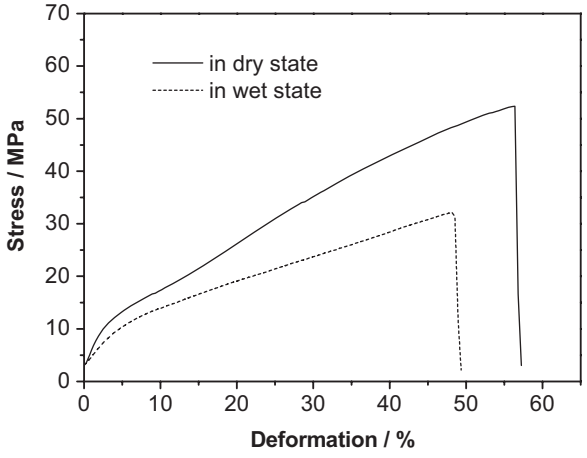

Figure 3. Stress/deformation curves of the PI@PVDF-HFP nonwovens in dry and wet states.

nanofibers. In order to further elucidate its mechanical property in devices, the tensile strength of the PI@PVDF-HFP nonwovens was also measured in wet state after being soaked in the liquid electrolyte for 2 h. It was founded that the PI@PVDF-HFP nonwoven exhibited reduced tensile strength of 31 MPa with deformation of 47% due to the gelation of the PVDF-HFP sheath layers in liquid electrolyte. It is well known that PVDF-HFP was widely reported as a gel polymer electrolyte in lithium ion battery, whereas the poor mechanical property after gelation hindered its extensive application.[13,32,33,35,36] In our case, the PI@PVDF-HFP nonwovens performed remarkable higher tensile strength of 31 MPa, which was almost as five times as that of the gelated PVDF-HFP membrane[35] and double that of the dip coating PE/PEO&PVDF-HFP membrane.[13] There is no doubt that the thermosetting PI core component mainly contributed to the mechanical reinforcement when the PVDF-HFP sheath layers gelated in liquid electrolyte. In regards of safety in electrode sheets stacking during battery assembly or accident collision, the PI@PVDF-HFP nonwoven separators will offer more reliable mechanical property, which is much better than the transverse strength of the Celgard separator. (Seen in Figure S5 of Supporting Information).

In comparison with the commercial Celgard 2500 separator (seen in Figure S2 of Supporting Information), the PI@PVDF-HFP nonwovens possessed higher porosity of 72%, extremely lower gurley value of 6.5 s and higher EU of 470%. It was shown in Figure S6 of Supporting Information that the nonwoven separator was rapidly wetted by the liquid electrolyte. This improvement in EU and wettability was attributed to the highly porous nanostructure and also the better affinity interaction between the PDVF-HFP segments and the liquid electrolyte.

The thermal shrinkage of separators is another important factor that determines the battery safety. The photographs of the PI@PVDF-HFP nonwovens and Celgard PP separator before and after thermal treatment at 150 °C for 1 h were presented in Figure 4. It could be seen that the PI@PVDF-HFP nonwovens did not shrink, while the Celgard 2500 separator shrank by 33% at the machine direction. The serious shrinkage of PP separator was originated from the stretching action during the fabrication.[1] According to the DSC analysis shown in Figure S7(a) of Supporting Information, PP and PVDF-HFP melt at around 160 and 140 °C, respectively, whereas the PI possesses superior thermal stability over 300 °C. Although the sheath layer of PVDF-HFP would melt at 140 °C shown in Figure S7(b) of Supporting Information, the thermosetting PI of core component retained intact and provided a stable host for the melting PVDF-HFP when above 140 °C. Actually, the PI@PVDF-HFP nonwoven separator was prepared via a thermal treatment at much higher temperature of 300 °C. Therefore, PI@PVDF-HFP nonwovens have great potential in high thermal stability separators for a high temperature condition.[37]

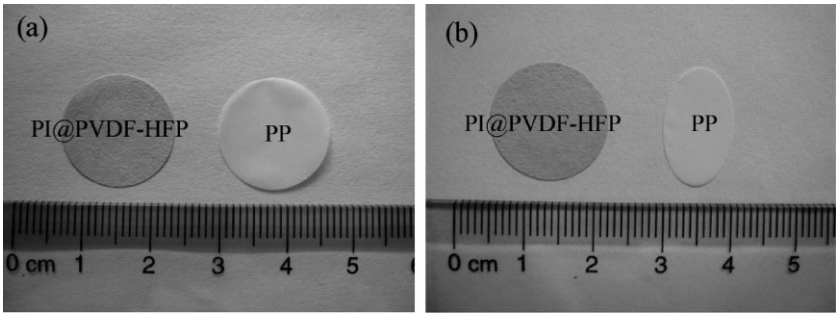

Figure 4. Photographs of the PP separator and PI@PVDF-HFP nonwoven (a) before and (b) after thermal treatment at 150 °C for 1 h.

3.3. Electrochemical Performance of the PI@PVDF-HFP Nonwoven sSeparators

The electrochemical stability window of the PI@PVDF-HFP nonwoven was measured from the linear sweep voltammograms. In Figure 5, it was depicted that the PI@PVDF-HFP nonwoven possessed better electrochemical stability window than the PP separator. The commercial carbonate electrolytes possess a decomposition voltage around 4.3 V vs. Li^+/Li probably due to trace impurity.[38] In our case, no obvious decomposition of carbonate electrolytes occurred below 5.2 V vs. Li^+/Li using PI@PVDF-HFP nonwoven as separators, which was attributed to the better electrolyte retention and electrochemical stability of PVDF-HFP sheath. It was deduced that the PI@PVDF-HFP separator could deliver a superior electrochemical stability and more favorable interface.

The ionic conductivity of liquid electrolyte-soaked PI@PVDF-HFP separator was 1.68 mS · cm^{-1} at 25 °C, 2.33 mS · cm^{-1} at 40 °C and 3.44 mS · cm^{-1} at 90 °C. Owing to the unique characteristic of high porosity, this PI@PVDF-HFP separator exhibited an excellent ionic conductivity close to that of PVDF-HFP electrolyte[35] and nearly double that of the PP one.[39]

$$\sigma(T) = A \cdot \exp(-E_a/RT) \quad (1)$$

$$\sigma(T) = A \cdot T^{-1/2} \cdot \exp(-E_a/R(T - T_0)) \quad (2)$$

A is a parameter indicative of the number of charge carriers, E_a is the activation energy of the activated ion-hopping conduction process, while T_0 is a parameter correlated to the glass transition temperature.[40]

The relationship of ln σ vs. $1/T$ curve was shown in Figure 6. These plots of ln σ vs. $1/T$ exhibit an obvious curvature,

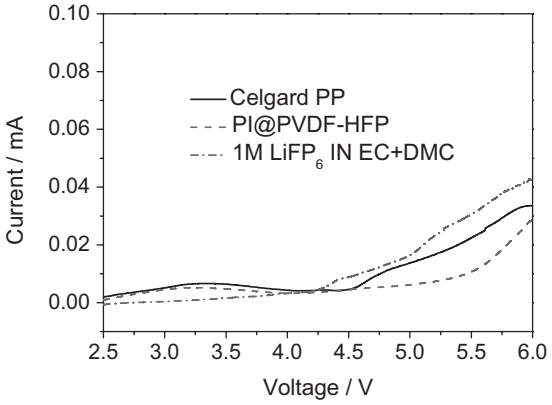

Figure 5. Linear sweep voltammograms of the liquid electrolyte, the PI@PVDF-HFP nonwoven separator and the PP separator at a scan rate of 1.0 mV · s^{-1}.

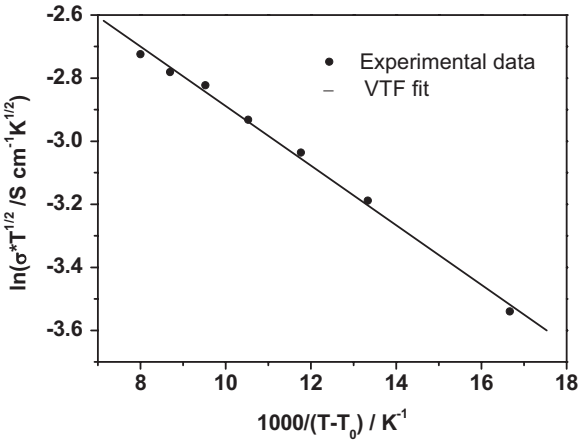

Figure 7. VTF plot of conductivity data for liquid electrolyte-soaked PI@PVDF-HFP nonwoven.

which did not agree with Equation 1 and this was characteristically indicative of a coupling between the ionic conductivity and the polymer chains dynamics.[40,41] Figure 7 showed the conductivity data plotted according to the Vogel-Tamman-Fulcher (VTF) empirical Equation 2, which displayed a linear behavior. The related parameters A, E_a and T_0 were calculated to be 0.143 ± 0.005 S · cm^{-1} · $K^{1/2}$, $(8.14 \pm 0.24) \times 10^{-3}$ eV and 238.15 ± 3 °C, respectively, by a non-linear-least square fitting regression on the experimental data.

Figure 8 depicts a comparison of the charge-discharge curves at the 0.5 C rate for the test cells using the Celgard separator and the PI@PVDF-HFP nonwoven separator. These cells showed stable charge-discharge curves with discharge capacities of about 125 and 130 mAh · g^{-1}, respectively (based on the weight of $LiCoO_2$). The stable voltage profiles would be partly ascribed to the electrochemical stability of the PI@PVDF-HFP separator.

Figure 9 showed rate capabilities of the cells with the PI@PVDF-HFP nonwoven separator and the PP separator. The cell with Celgard 2500 showed specific capacity about 131 mAh · g^{-1} based on the weight of $LiCoO_2$ at 0.2 C discharge and the capacity decreased rapidly to 95 mAh · g^{-1} at 4 C and 76 mAh · g^{-1} at 8 C rate. Nevertheless, for the cell with the nonwoven, the capacity kept 116 mAh · g^{-1} at 4 C and 100 mAh · g^{-1} at 8 C rate, respectively. The chosen Celgard 2500 here was ever reported to perform the best in high rate capability tests among the Celgard separators.[39] Obviously, our PI@PVDF-HFP separator performed better rate capability than the chosen Celgard 2500. This is because that PI@PVDF-HFP separator possesses higher porosity and higher ionic

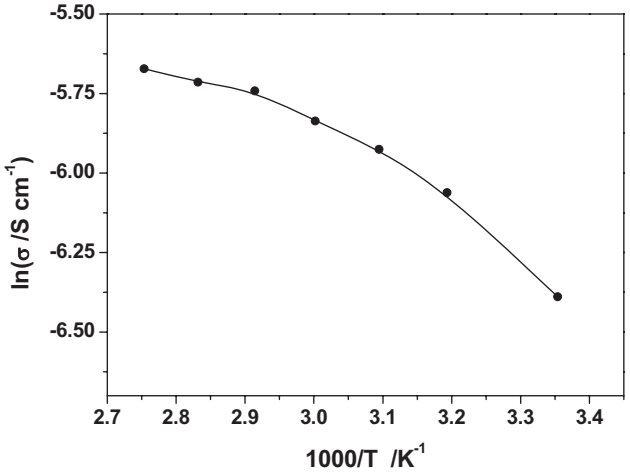

Figure 6. Arrhenius plot of conductivity data for liquid-electrolyte-soaked PI@PVDF-HFP nonwoven separator.

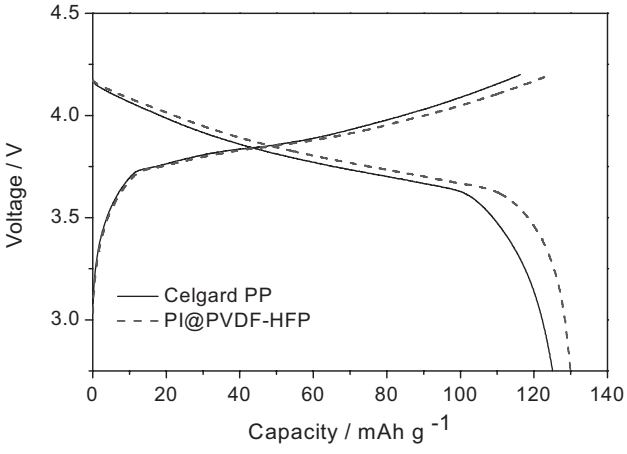

Figure 8. Charge/discharge curves for the cells using the PP separator and the PI@PVDF-HFP nonwoven separator at 0.5 C rate.

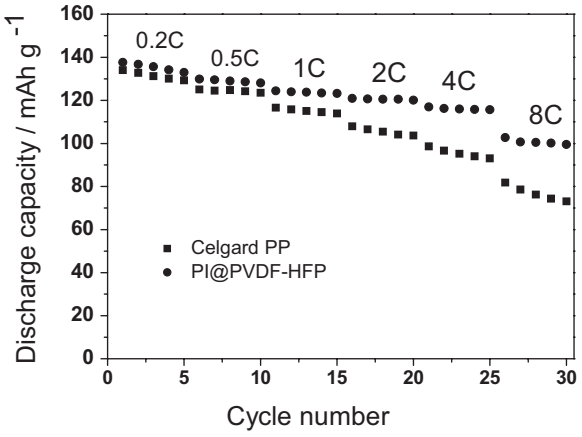

Figure 9. Rate capabilities of the cells using PP separator and PI@PVDF-HFP nonwoven separator.

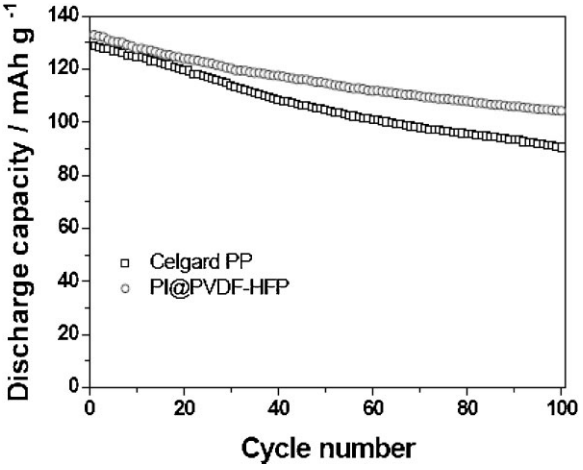

Figure 10. Discharge capabilities vs. cycle number of the cells using the PP separator and the PI@PVDF-HFP nonwoven separator.

conductivity. The cycle stability of the cell with PI@PVDF-HFP separator was displayed in Figure 10 at charge/discharge rate of 0.5 C. The obtained discharge capacity after 100 cycles was around 105 mAh $\cdot$ g^{-1} indicative of capacity retention at 81% better than 69% of Celgard 2500. It was manifested that our nonwoven separator exhibited relatively better cycling performance than the Celgard 2500 under the same condition, which was ascribed to the better liquid-electrolyte affinity and retainability of the PVDF-HFP sheath.

4. Conclusion

The composite PI@PVDF-HFP nanofibrous separators had been fabricated by coaxial electrospinning technique with considerable mechanical strength and thermal stability. Compared to the commercialized microporous PP separator, the PI@PVDF-HFP nonwoven possessed higher porosity, extremely lower gurley value, better affinity to electrolyte and higher EU. It was also demonstrated that the cell with the PI@PVDF-HFP nonwovens performed much better rate capabilities and improved capacity retention. These superior mechanical, thermal stability and high rate capability endowed this composite nonwoven a promising alternative to the conventional PP separators in high-power lithium ion batteries. Moreover, the PI@PVDF-HFP nonwovens behaved like a robust gel polymer electrolyte, which may be potential application for the high temperature batteries. All these signify that it is a promising technique to fabricate high performance separators or electrolytes by this coaxial electrospinning.

5. Supporting Information

Supporting information is available from the Wiley Online Library or from the author. This includes the scheme of synthesis of the polyimide and its precursor, the illustrated size configuration of the tip of the spinneret, the typical SEM image of the Celgard 2500 separator and its stress-deformation curves at the transverse direction, typical SEM images of the PI@PVDF-HFP nanofibers at different sheath solution feed rates, typical SEM images of the nanofibers cross sections after being quenched in liquid nitrogen, photographs of the PI@PVDF-HFP and Celgard 2500 separators contacting liquid electrolyte and their DSC traces.

Acknowledgements: This work was supported by the Instrument Developing Project of the Chinese Academy of Sciences (No. YZ201137), the '100 talents' program of the Chinese Academy of Sciences, the National Program on Key Basic Research Project of China (973 Program) (No. MOST2011CB935700), the National Natural Science Foundation (No. 20971077, 20901044 and 20902052) and Shangdong Province Fund for Distinguished Young Scientist (No. JQ200906).

Received: May 2, 2012; Revised: July 3, 2012; Published online: September 19, 2012; DOI: 10.1002/mame.201200158

Keywords: coaxial electrospinning; fibers; lithium ion batteries; nanocomposites; separators

[1] P. Arora, Z. G. Zhang, *Chem. Rev.* **2004**, *104*, 4419.
[2] S. S. Zhang, *J. Power Sources* **2007**, *164*, 351.
[3] J. Hassoun, S. Panero, B. Scrosati, *J. Mater. Chem.* **2007**, *17*, 3668.

[4] H. Li, Z. X. Wang, L. Q. Chen, X. J. Huang, *Adv. Mater.* **2009**, *21*, 4593.
[5] M. R. Palacin, *Chem. Soc. Rev.* **2009**, *21*, 2565.
[6] M. H. Ryou, Y. M. Lee, J. K. Park, J. W. Choi, *Adv. Mater.* **2011**, *23*, 3066.
[7] J. Y. Kim, D. Y. Lim, *Energies* **2010**, *3*, 866.
[8] M. Kim, J. Y. Shon, Y. C. Nho, T. W. Lee, J. H. Parka, *J. Electrochem. Soc.* **2010**, *157*, A31.
[9] T. H. Cho, M. Tanaka, H. Onishi, Y. Kondo, T. Nakamura, H. Yamazaki, S. Tanase, T. Sakai, *J. Power Sources* **2008**, *181*, 155.
[10] S. H. Yoo, C. K. Ki, *Ind. Eng. Chem. Res.* **2009**, *48*, 9936.
[11] Y. S. Chung, S. H. Yoo, C. K. Kim, *Ind. Eng. Chem. Res.* **2009**, *48*, 4346.
[12] H. Yoneda, Y. Nishimura, Y. Doi, M. Fukuda, M. Kohno, *Polym. J.* **2010**, *42*, 425.
[13] Y. H. Liao, X. P. Li, C. H. Fu, R. Xu, L. Zhou, C. L. Tan, S. J. Hu, W. S. Li, *J. Power Sources* **2011**, *196*, 2115.
[14] T. H. Cho, M. Tanaka, H. Ohnishi, Y. Kondo, M. Yoshikazu, T. Nakamura, T. Sakai, *J. Power Sources* **2010**, *195*, 4272.
[15] T. H. Cho, M. Tanaka, H. Onishi, Y. Kondo, T. Nakamura, H. Yamazaki, S. Tanase, T. Sakaia, *J. Electrochem. Soc.* **2008**, *155*, A699.
[16] T. H. Cho, T. Sakai, S. Tanase, K. Kimura, Y. Kondo, T. Tarao, M. Tanaka, *Electrochem. Solid State Lett.* **2007**, *10*, A159.
[17] Y. Z. Liang, L. W. Ji, B. K. Guo, Z. Lin, Y. F. Yao, Y. Li, M. Alcoutlabi, Y. P. Qiu, X. W. Zhang, *J. Power Sources* **2011**, *196*, 436.
[18] E. S. Choi, S. Y. Lee, *J. Mater. Chem.* **2011**, *21*, 14747.
[19] H. S. Jeong, J. H. Kim, S. Y. Lee, *J. Mater. Chem.* **2010**, *20*, 9180.
[20] J. H. Cho, J. H. Park, J. H. Kim, S. Y. Lee, *J. Mater. Chem.* **2011**, *21*, 8192.
[21] D. Bansal, B. Meyer, M. Salomon, *J. Power Sources* **2008**, *178*, 848.
[22] Y. Wang, H. Y. Zhan, J. Hu, Y. Liang, S. S. Zeng, *J. Power Sources* **2009**, *189*, 616.
[23] J. J. Miao, M. Miyauchi, T. J. Simmons, J. S. Dordick, R. J. Linhardt, *J. Nanosci. Nanotechnol.* **2010**, *10*, 5507.
[24] I. G. Locertales, A. Barrero, I. Guerrero, R. Cortijo, M. Marquez, A. M. Ganan-Calvo, *Science* **2002**, *295*, 1154.
[25] Z. C. Sun, E. Zussman, A. L. Rarin, J. H. Wendorff, A. Greiner, *Adv. Mater.* **2003**, *15*, 1929.
[26] G. Kwak, G. H. Lee, S. H. Shim, K. B. Yoon, *Macromol. Rapid Commun.* **2008**, *29*, 815.
[27] M. Lallave, J. Bedia, R. Ruiz-Rosas, J. Rodríguez-Mirasol, T. Cordero, J. C. Otero, M. Marquez, A. Barrero, I. G. Loscertales, *Adv. Mater.* **2007**, *19*, 4292.
[28] C. Wang, K. W. Yan, Y. D. Lin, P. C. H. Hsieh, *Macromolecules* **2010**, *43*, 6389.
[29] J. T. McCann, M. Marquez, Y. Xia, *Nano Lett.* **2006**, *6*, 2868.
[30] a) Y. Z. Zhang, Z. M. Huang, X. J. Xu, C. T. Lim, S. Ramakrishna, *Chem. Mater.* **2004**, *16*, 3406; b) X. L. Xu, X. L. Zhuang, X. S. Chen, X. R. Wang, L. X. Yang, X. B. Jing, *Macromol Rapid Commun.* **2006**, *27*, 1637.
[31] M. Wei, J.S. Lee, B.W. Kang, J.,* Mead, *Macromol. Rapid Commun.* **2005**, *26*, 1127.
[32] S. W. Choi, S. M. Jo, W. S. Lee, Y. R. Kim, *Adv. Mater.* **2003**, *15*, 2027.
[33] X. Li, G. Cheruvally, J. K. Kim, J. W. Choi, J. H. Ahn, K. W. Kim, H. Ahn, *J. Power Sources*, **2007**, *167*, 491.
[34] C. B. Huang, S. Q. Wang, H. A. Zhang, T. T. Li, S. L. Chen, C. L. Lai, H. Q. Hou, *Eur. Polym. J.* **2006**, *42*, 1099.
[35] Z. Jiang, B. Carroll, K. M. Abraham, *Elecrrochim. Acta* **1997**, *42*, 2667.
[36] A. I. Gopalan, P. Santhosh, K. M. Manesh, J. H. Nho, S. H. Kim, C. G. Hwang, K. P. Lee, *J. Membr. Sci.* **2008**, *325*, 683.
[37] F. Mestre-Aizpurua, S. Hamelet, C. Masquelier, M. R. Palacin, *J. Power Sources* **2010**, *195*, 6897.
[38] K. Xu, *Chem. Rev.* **2004**, *104*, 4303.
[39] D. Djian, F. Alloin, S. Martinet, H. Lignier, J. Y. Sanchez, *J. Power Sources*, **2007**, *172*, 416.
[40] F. Croce, M. L. Focarete, J. Hassoun, I. Meschinia, B. Scrosat, *Energy Environ. Sci.* **2011**, *4*, 921.
[41] N. Kaskhedikar, Y. Karatas, G. L. Cui, J. Maier, H. D. Wiemhöfer, *J. Mater. Chem.* **2011**, *21*, 11838.